Slow Sound Phenomena Caused by Frame Shrinkage in Square Frame Acoustic Metafluid

Dongliang Pei, Zixian Cui, Ping Xiang and Xiaodong Ding

China Shipbuilding Corporation System Engineering Research Institute, Beijing, 100080, China. E-mail: 1454426832@qq.com

Yangyang Chu

College of Software Engineering, Zhengzhou University of Light Industry, Zhengzhou 450001, China.

(Received 26 March 2024; accepted 25 July 2024)

The present study investigates the equivalent bulk modulus and density of square frame underwater acoustic metafluid (AMF) cells with four distinct frame forms. It is observed that, besides frame thickness, a certain degree of shrinkage at the center of the frame also influences the equivalent parameters of cells. Specifically, this shrinkage leads to a decrease in the equivalent volume modulus and an increase in the equivalent density, ultimately resulting in the slow sound velocity phenomenon of the cell. The frame shrinkage causes part of the air to be replaced, resulting in an increase in density. At the same time, it makes the cell more prone to "shrink and expand" type volume deformation, resulting in the reduction of volume modulus. Finally, an impedance-matched slow sound velocity (0.5 times) metafluid cell is designed by frame shrinkage and verified by analyzing the transmission effect of a waveguide containing 20 cells and the sound pressure distribution at different positions in the waveguide.

1. INTRODUCTION

Over the past few decades, there has been a growing interest in acoustic metamaterials. These materials possess unique properties that have led to the development of various applications, such as acoustic focusing, communication, and stealth capabilities.[1–12] As more advanced acoustic cells are proposed, the potential application range of acoustic metamaterials continues to expand. In 1968, Veselago introduced the concept of metamaterials to describe artificially synthesized periodic or aperiodic composites with properties determined by specially designed material cells,[13] offering the possibility of controlling material properties through cell design. Acoustic metamaterials can be classified into resonant and non-resonant types. Resonant metamaterials often utilize resonance phenomena like local, helmholtz, and thin film resonance to achieve extraordinary dynamic equivalent parameters such as negative mass density, negative volume modulus, negative refractive index, zero refractive index, etc.[14–19] However, due to limitations imposed by resonance principles, these extraordinary parameters typically exhibit narrow frequency bands.[20–22] To realize wideband acoustic metamaterial, researchers have turned their attention toward pentamode acoustic metamaterials.[23–30] Pentamode materials (PM) are unique solid acoustic metamaterials characterized by a high ratio of equivalent bulk modulus to equivalent shear modulus, resulting in significant shear deformation relative to volume deformation. Some scholars also refer to PM as acoustic metafluid.[31,32] In 2011, Norris designed a two-dimensional pentamode unit cell featuring a regular hexagonal frame and a rectangular counterweight at six vertices to adjust the density.[33] Subsequently, numerous scholars have modified this structure and developed various wideband cells based on pentamode metamaterials. In 2015, Tian et al. utilized a pentamode unit cell to design a hydroacoustic metasurface. By leveraging the excellent broadband characteristics of the pentamode material and its impedance-matching properties with the environmental medium, eight different pentamode unit cells were designed following the generalized Snell law, resulting in the realization of a dispersion-free design that operates over a wide frequency range. Chen et al., through simulation and experimentation, designed a layered ring acoustic cloak that demonstrated its effectiveness across a broad band range.[34] In 2019, Chen et al. successfully created and produced pentamode materials that verified broadband conversion from underwater cylindrical waves to plane waves through experimental validation.[35] Cushing et al. devised an aluminum-based metal gradient refractive index acoustic lens, which showed improvement in reducing aberrations through underwater experiments.[36] Zhang et al., utilizing the generalized Snell law, developed a wideband reflective metasurface based on pentamode materials capable of reflecting and deflecting vertically incident sound waves by 15° within the frequency range of $6-18$ kHz.[37]

For a pentamode unit cell, the thickness of the frame primarily influences the equivalent volume modulus of the cell, with a smaller thickness resulting in a lower volume modulus. The various counterweights within a unit cell mainly impact its equivalent mass density. In traditional pentamode cells, the frame and counterweight are made from the same material, leading to significant coupling between their equivalent density and volume modulus. This limitation hinders the design and processing of such unit cells. Subsequently, some scholars proposed an improved pentamode unit cell incorporating two/three phases by introducing a soft connecting layer between the frame and counterweight to reduce this coupling effect.[38] This improvement reduces manufacturing costs and minimizes the processing time consumed to construct these pentamode cells. Overall, although static design

allows for a gradual approximation of fluid behavior in pentamode unit cells, it remains challenging to eliminate their small shear modulus. Consequently, ensuring dynamic performance similar to water becomes difficult and affects the broadband capabilities of these cells.[23] In 2022, Zhou et al. designed an underwater carpet cloak using a three-component metafluid composed of syntactic foam, steel, and water that works well under both normal and oblique incidences for broadband frequencies.[39] Jun Yang et al. recently designed a metamaterial cell consisting of a solid metal frame immersed in water to eliminate shear wave components within this metamaterial system. Their findings indicate that occupancy primarily affects its equivalent density while the number of sides and thickness of the frame influence its equivalent bulk modulus. By adjusting parameters such as the number of sides, materials used, and filling rate within the frame structure itself, independent control over both equivalent density and equivalent volume modulus can be achieved for underwater metafluids.[40]

Therefore, whether in the design of pentamode metamaterials or underwater metafluids, the thickness of the frame plays a crucial role in determining the equivalent volume modulus of a unit cell. A smaller frame thickness results in a lower equivalent volume modulus. By adjusting the equivalent density, achieving a higher equivalent refractive index for impedance matching metamaterials is possible, which can significantly enhance the performance of cells.[34] However, achieving a thin frame thickness is often challenging during production due to expensive and time-consuming WEDM-LS (Low-Speed Wire Electrical Discharge Machining), water-jet cutting techniques, and the lattice structure cut from a whole massive block.[38] On the basis of keeping the frame thickness unchanged or thickened, how to make the equivalent volume modulus of a single cell lower or unchanged has become a difficult problem in the design of acoustic metamaterials for low-cost manufacturing. In this paper, through analyzing four different parameterized metafluid unit cells' equivalent parameters, it is discovered that introducing some amount of shrinkage into unit cell frames may provide insights towards solving this challenging problem.

2. MAIN RESULTS

The cell depicted in Fig. 1(a) was initially proposed by Bi[40] and is referred to as a metafluid unit cell. Based on this design, this study establishes four distinct unit cells, and their structural forms are illustrated in Figs. 1(a)–1(d). The unit cell shown in Fig. 1(a) corresponds to the minimum volume modulus design described in the literature.[40] The remaining unit cells are derived from modifications made to the form of it. The overall shape of the unit cell is square, with water occupying the outer blue area, a metal frame material constituting the inner gray area, and air filling up the innermost white region. The unit cell has a side length of $a = 13.5$ mm, with the distance between the center of the cell and the corner of the frame being $r = 7.1$ mm and the frame thickness of $h = 0.5$ mm. The frame is made of aluminum, with material parameters $\rho = 2700$ kg/m^3, $E = 70$ GPa, $\mu = 0.33$. In Fig. 1(b), the frame thickness of the unit cell is increased to $h = 0.65$ mm while keeping other parameters unchanged from Fig. 1(a). Figure 1(c) is obtained by shrinking the center of the outer side of the frame based on Fig. 1(a). A new variable called shrinkage factor $s = (x - x_s)/x$ is defined here, which represents the ratio of the difference between the horizontal distance from the center of the point on the right side of the square before (x) and after (x_s) shrinkage to before (x). When s is equal to $1/3$, we obtain Fig. 1(c). Furthermore, in Fig. 1(d), an increase in frame thickness to $h = 0.65$ mm is applied based on Fig. 1(c). In this paper, Figs. 1(a)–1(d) are referred to as AMF1-AMF4 respectively, for convenience purposes, and their structural parameters are listed in Table 1.

The low-frequency equivalent parameters of the cell are focused mainly here. In the long wavelength condition, according to the equivalent medium theory, the equivalent mass density of a unit cell is the average area density of the material constituting the unit cell, expressed as ρ_{eff}. The equivalent bulk modulus is obtained according to the formula $B_{eff} = \rho_{eff} * c_{eff}^2$, where B_{eff} is the equivalent bulk modulus of the metafluid and c_{eff} is the equivalent sound velocity. The c_{eff} of a cell can be determined by calculating the slope of its band curve at a low-frequency range.[23] In order to obtain the band curves, the geometric model of the cell is established by using COMSOL Multiphysics software. The solid mechanical physical field was set as the frame structure, while the pressure acoustic physical field represented water and air areas. The boundary between these two fields served as an acoustic-solid coupling boundary. The Floquet boundary condition is set on the opposite side of a unit cell, and the band curves of AMF1-AMF4 can be obtained by parametric scanning along the boundary of the irreducible Brillouin zone of a unit cell (M-Γ-X-M in the lower left corner of Fig. 1(a)), as illustrated in Fig. 2.

The band curve of AMF1 in Fig. 2(a) demonstrates the consistent stability of the sound velocity within the frequency range of $0-10$ kHz. However, a notable "segmentation" effect is observed on this initially stable curve between $5-8$ kHz. To investigate this phenomenon further, we have specifically chosen to analyze three characteristic frequencies located at position 0.1ΓX; these specific frequencies are represented by points A, B, and C as shown in Fig. 2(a). Correspondingly illustrated in Figs. 3(a)–3(c) are vibrational modes associated with these points. As shown by the arrows in Fig. 3(a), the vibration form of the unit cell corresponds to the translational motion of the frame combined with contract expansion deformation, representing the compression wave mode as its lowest-order vibration form along the ΓX direction. This distinguishes it from traditional solid phase pentamode metamaterials dominated by shear wave modes due to their inherent shear modulus, which is challenging to eliminate. However, with water serving as its outer layer, our designed unit cell effectively eliminates any presence of shear wave modes. Moving on to Fig. 3(b), we observe a similar vibration form for the unit cell resembling a local resonance mode known as quadrupole described in literature references.[14,16,17,19] Specifically, it involves relative motion between an opposite straight rod "mass" and an opposite vibration phase for adjacent straight rods. The vibration pattern shown in Fig. 3(c) exhibits similarities to that depicted in Fig. 3(b), except for the fact that the "mass" transforms into a curved bar with right angles. As a result, B and C represent local resonance modes, while A means a compression wave mode.

In comparison to AMF1, the band of the AMF3 is illustrated in Fig. 2(c). The first three orders at position 0.1ΓX are se-

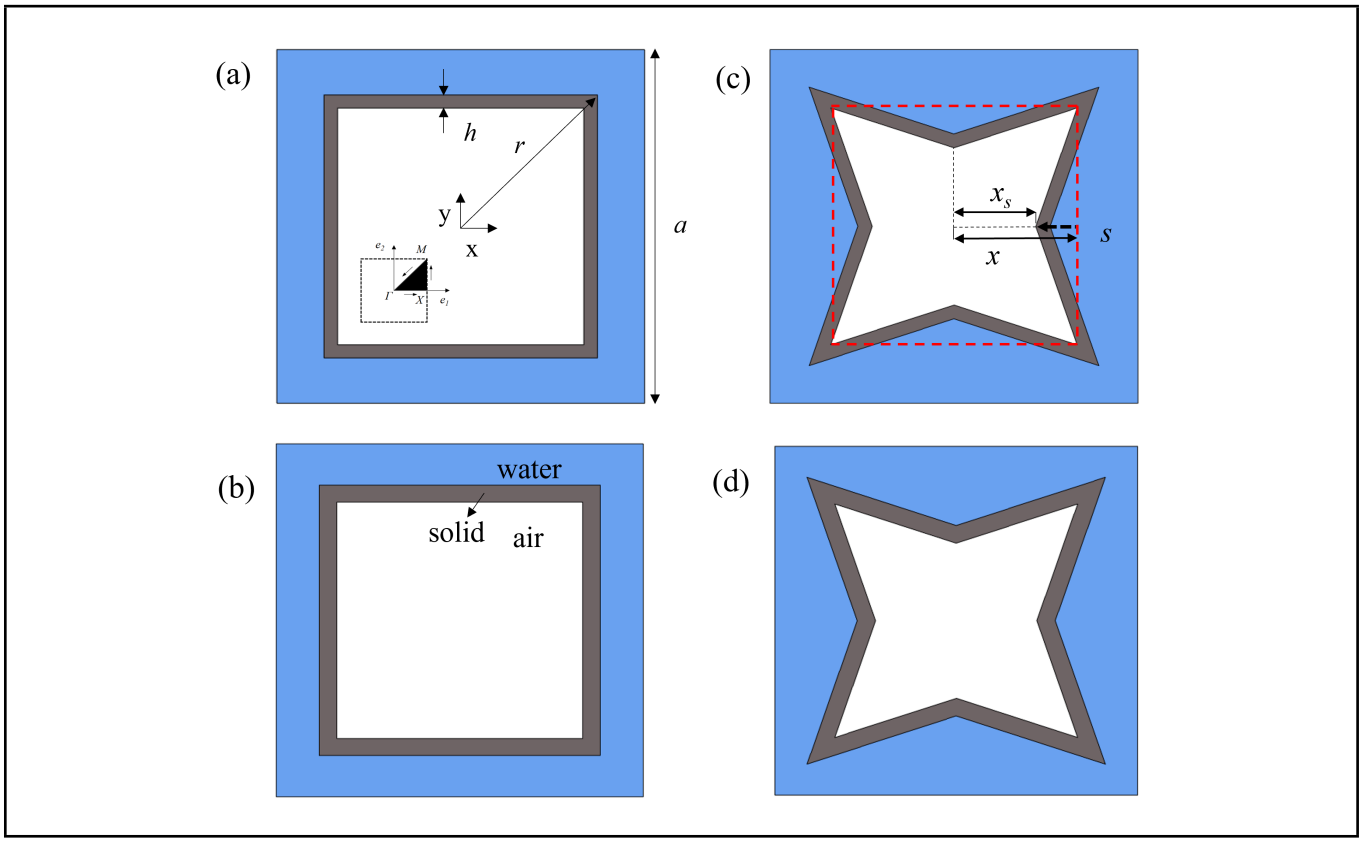

Figure 1. Four unit cells with varying structural parameters. (a) A primary unit cell features a hollow square frame immersed in water and exhibiting a square shape. The illustration depicts the first Brillouin zone (marked by the dashed lines) and the irreducible Brillouin zone M-Γ-X-M (denoted by the shaded region) of the square lattice; (b) Increasing the thickness of the frame by 30% based on cell (a); (c) Introducing shrinkage factor $s = (x - x_s)/x$ to (a), where x represents the horizontal coordinate of the point before shrinkage, and x_s represents the horizontal coordinate after shrinkage; (d) Increasing the thickness of the frame by 30% based on (c). The four unit cells corresponding to (a)-(d) are denoted as AMF1-AMF4, respectively.

lected for analysis, corresponding to intersection points D, E, and F on the black dotted line intersecting with the band curve in Fig. 2(c). The vibration modes are displayed in Figs. 3(d)–3(f). It can be observed that the first characteristic mode of AMF3 resembles that of AMF1 as a compression wave vibration mode; however, its corresponding frequency is lower. The second characteristic mode corresponds to the third vibrational pattern in AMF1 and possesses a comparable frequency. The third distinct mode corresponds to the second vibrational pattern identified in AMF1 but displays an upward shift in its frequency. Therefore, for the AMF cells in this paper, the first vibration mode of its band curve is the compression wave mode. Some narrow frequency bands with quadrupole local resonance modes often appear in the wide band compression wave. Then, we focus on the compression wave mode of the band curve and ignore the local resonance mode in the narrow band. So, two compression wave curves starting from Γ were observed on each band curve with different slopes at low frequencies indicated by red dashed lines in Fig. 2; their slope represents c_{eff} for the cell. By comparing the slope of AMF3 and AMF1, it can be seen that the equivalent ompression wave sound velocity of AMF3 is smaller than that of AMF1.

Through the previous analysis, we can obtain the equivalent sound velocity and equivalent density of a cell. The obtained equivalent parameters of AMF1-AMF4 are summarized in Table 1. Firstly, a comparative analysis is conducted from the equivalent density. The frame thickness of AMF2 is greater than that of AMF1, resulting in a higher equivalent density. Compared with AMF1, the presence of a certain shrinkage factor leads to an increase in density for AMF3 as it replaces air with metal and water. Formed by shrinkage based on AMF2, AMF4 exhibits an even higher equivalent density than both AMF2 and greater than AMF1. Therefore, the relative equivalent density is arranged in increasing order: AMF1, AMF2, AMF3, and AMF4.

Table 1. Parameters related to the four unit cell.

	Frame thickness h (mm)	Shrinkage factor s	Relative equivalent density	Relative equivalent sound velocity	Relative equivalent volume modulus
AMF1	0.5	0	0.73	0.46	0.15
AMF2	0.65	0	0.79	0.61	0.29
AMF3	0.5	0.33	0.89	0.27	0.07
AMF4	0.65	0.33	0.96	0.37	0.13

Next, the analysis focuses on the relative equivalent volume modulus. For a two-dimensional unit cell, the effective bulk modulus B_{eff} of the cell can be expressed as:

$$\frac{1}{B_{eff}} = \frac{1}{a^2}\left(\frac{S_w}{B_w} + \frac{dS_{solid}}{dP}\right); \tag{1}$$

where a is the side length of the cell, S_w and B_w are the area fraction of water and the bulk modulus of water. dS_{solid}/dP is the relative decrease of the area from the solid frame under isotropic pressure. According to the analysis in reference,[40] the reduction of unit cell area under pressure dP can be attributed to two factors: firstly, an overall decrease in the polygonal frame; secondly, a reduction in area caused by bending deformation of each beam of the frame. dS_{solid}/dP increases

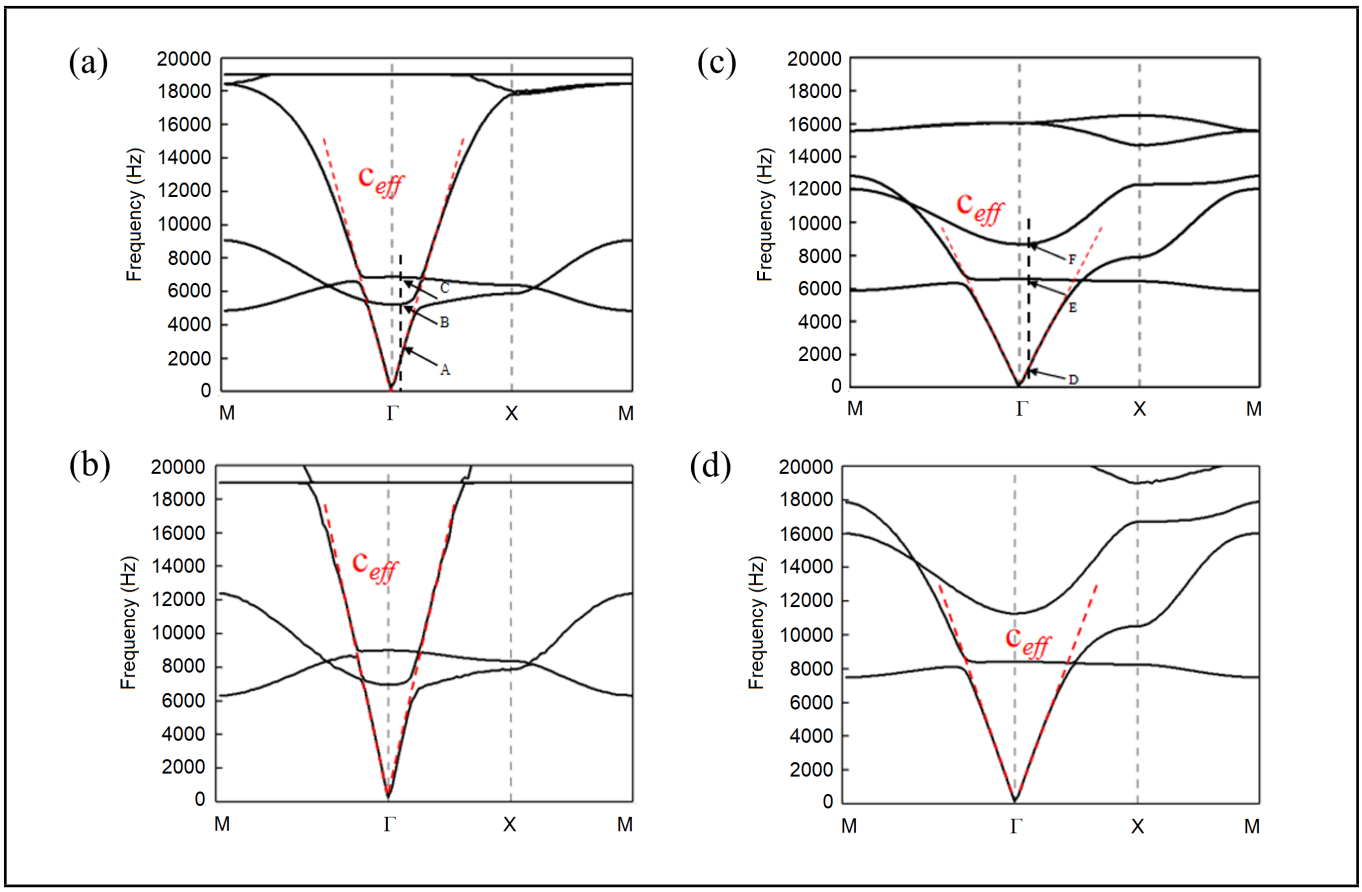

Figure 2. The band curves and related characteristics of the four cells. (a) The band curve of AMF1. The position corresponding to the black dashed line represents a wave vector position of 0.1ΓX, and the first three intersections between this line and the band curve are defined as points A, B, and C, respectively. The red dashed line represents a unit cell's compression wave sound velocity curve. (b) The band curve of AMF2. (c) The band curve of AMF3. The position corresponding to the black dashed line represents a wave vector position of 0.1ΓX, and the first three intersections between this line and the band curve are defined as points D, E, and F, respectively. (d) The band curve of AMF4.

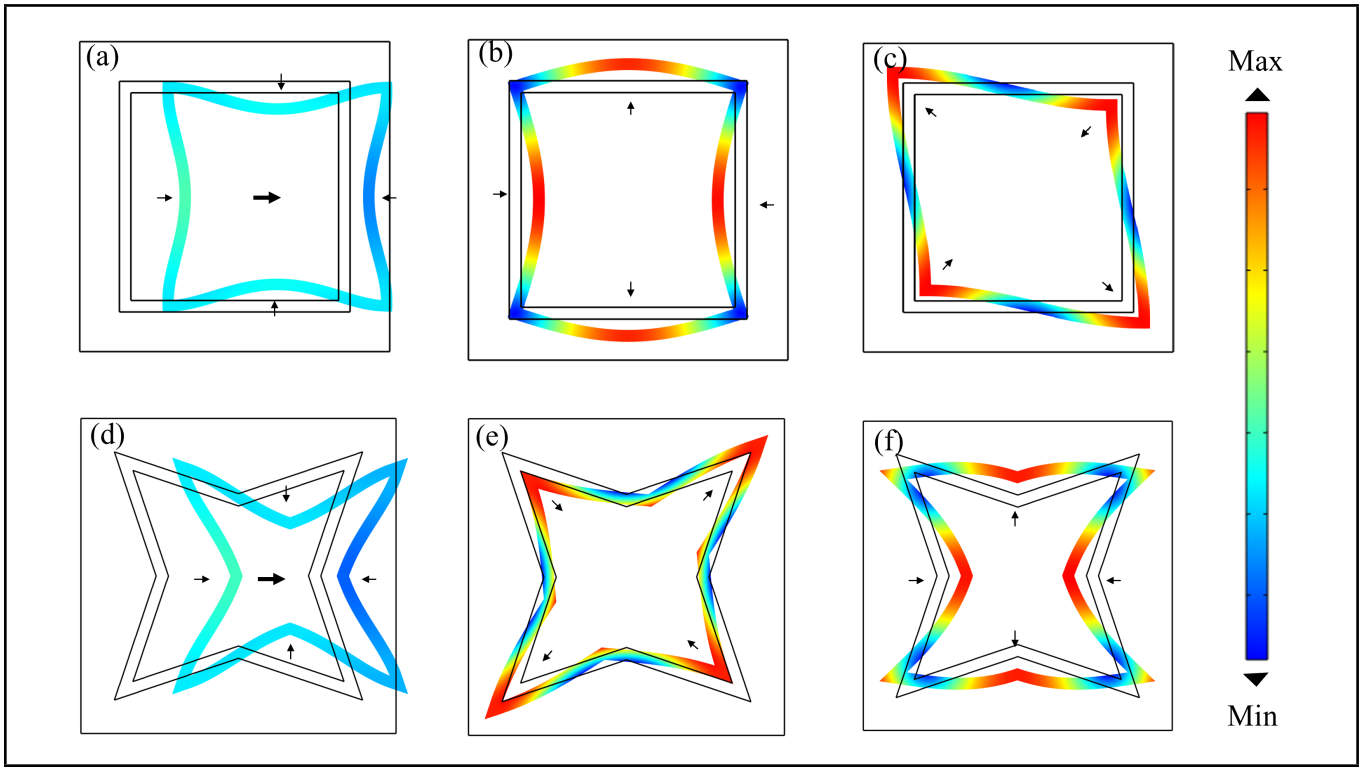

Figure 3. The vibration modes of unit cells at specific characteristic frequencies. Panels (a)-(f) depict the vibration displacement distribution at six positions A-F, as indicated in Fig. 2. The arrows show the direction of movement of the cell. In the legend, blue represents small displacement, while red indicates large displacement.

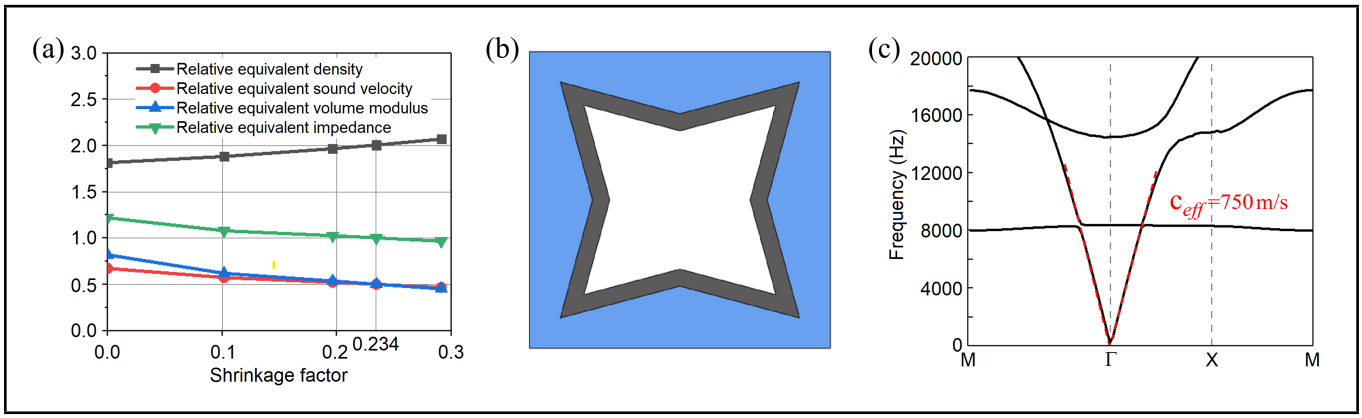

Figure 4. (a) Variation curves of different equivalent parameters of the cell are depicted concerning the shrinkage factor. The cell exhibits a gradual impedance-matching effect when $s = 0.245$. (b) Cell of the slow cell when $s = 0.245$. (c) The band curve is presented, where the red dotted line represents an equivalent sound speed of 750 m/s.

with the decrease of h and the increase of beam length. Consequently, the equivalent volume modulus B_{eff} of a cell increases with increasing h but decreases with increasing beam length and S_w.

The frame thickness of AMF2 surpasses that of AMF1, thus yielding a larger relative equivalent volume modulus. As shown in Table 1, the frame thickness of AMF2 (AMF1) is 0.65 mm (0.5 mm) and the relative bulk modulus of AMF2 is about 2 times of AMF1. Then we compare AMF3 with AMF1. Due to a certain shrinkage factor ($s = 0.33$), the beam length and the area fraction of water S_w of AMF3 is larger than AMF1, so the volume modulus for AMF3 should be smaller than AMF1. It can be seen from Table 1 that the relative bulk modulus of AMF3 is 0.07 and AMF1 is 0.15. The bulk modulus of AMF3 is less than half of that exhibited by AMF1. A similar trend can be observed when comparing AMF4 and AMF2 due to the shrinkage factor. In addition, the density of AMF3 is higher than that of AMF1, so its compression wave velocity must be smaller (0.27 versus 0.46). Finally, by comparing the structural characteristics and equivalent parameters of AMF1 and AMF4 from Table 1, it can be observed that while AMF4 possesses a thicker frame thickness, its relative equivalent bulk modulus and relative equivalent sound velocity remains slightly lower than that of AMF1 due to frame shrinkage. Therefore, the frame shrinkage of the AMF cell makes it more prone to shrinkage-expansion deformation, resulting in a decrease in both equivalent volume modulus and equivalent sound velocity.

As frame thickness increases, the cell's equivalent density and volume modulus rise concurrently. Introducing a shrinkage factor elevates cell density while diminishing its volume modulus. Shrinkage factor and frame thickness similarly affect cell density but have opposing impacts on its volume modulus. Therefore, for underwater metafluid cell design purposes, employing a shrinkage factor to reduce or maintain an equalized volume modulus while increasing frame thickness would facilitate easier fabrication of acoustic metamaterials. By augmenting frame thickness in thin metamaterial cells close to machining limits, comparable acoustic performance can be achieved without compromising machining accuracy or encountering issues with unmachinability.

Finally, an impedance-matched metafluid unit cell with sound velocity 0.5 times that of water is designed by exploiting the phenomenon of reduced bulk modulus caused by frame shrinkage, as shown in Fig. 4(b). The selected frame material, in this case, is a copper alloy (density $\rho = 8900$ kg/m^3, Young's modulus $E = 136$ GPa, and Poisson's ratio $\mu = 0.2$). When the cell remains unshrunk, the structural parameter is $r = 6.18$ mm, and the thickness is $h = 0.75$ mm. At this stage, the cell exhibits a relative equivalent density of 1.81 and a relative equivalent volume modulus of 0.82. Based on previous analysis, it can be concluded that the shrinkage factor enhances the equivalent density of the cell and reduces its equivalent volume modulus, thereby providing favorable conditions for constructing impedance-matched slow sound materials.

The shrinkage factor's impact on the cell's equivalent parameters is thoroughly analyzed in Fig. 4(a). The gray dotted line represents its influence on the equivalent density, while the red dotted line represents its effect on the equivalent sound velocity. Additionally, the blue dotted line signifies its impact on the equivalent volume modulus, and the green dotted line indicates its effect on the equivalent impedance. As depicted in Fig. 4(a), as the shrinkage factor s gradually increases from 0 to 0.31, several changes occur: firstly, there is a gradual increase in the equivalent density; secondly, there is a gradual decrease in both the equivalent volume modulus and sound velocity; lastly, there is also a gradual decrease in impedance from approximately 1.25. When s reaches around 0.245, specific values are observed: an equivalence density of exactly 2 for cells, an equivalence sound velocity of precisely 0.5, water-matching impedance, and an equivalence volume modulus of exactly 0.5. Figure 5(b) illustrates their structural form at this point while Fig. 4(c) displays their corresponding band curve. It reveals the presence of a resonance mode in the cell around 8 kHz, while the low-frequency band preceding 8 kHz exhibits a stable and broad slow sound speed effect.

To validate the dynamic characteristics of impedance-matched slow sound cells, an acoustic waveguide comprising 20 cells was constructed using COMSOL Multiphysics software (as illustrated in Fig. 5(a)). The dimensions of the waveguide are 13.5 mm × 880 mm. The plane wave is incident from the left side of the waveguide, then propagates through the cell array, and exits from the right side. Radiation boundaries are implemented at both ends to prevent acoustic reflection, while periodic boundaries are set for upper and lower boundaries. By evaluating the cell arrays' reflected and transmitted sound pressure and comparing them with the incident waves, we can determine the reflection and transmission coefficients of the

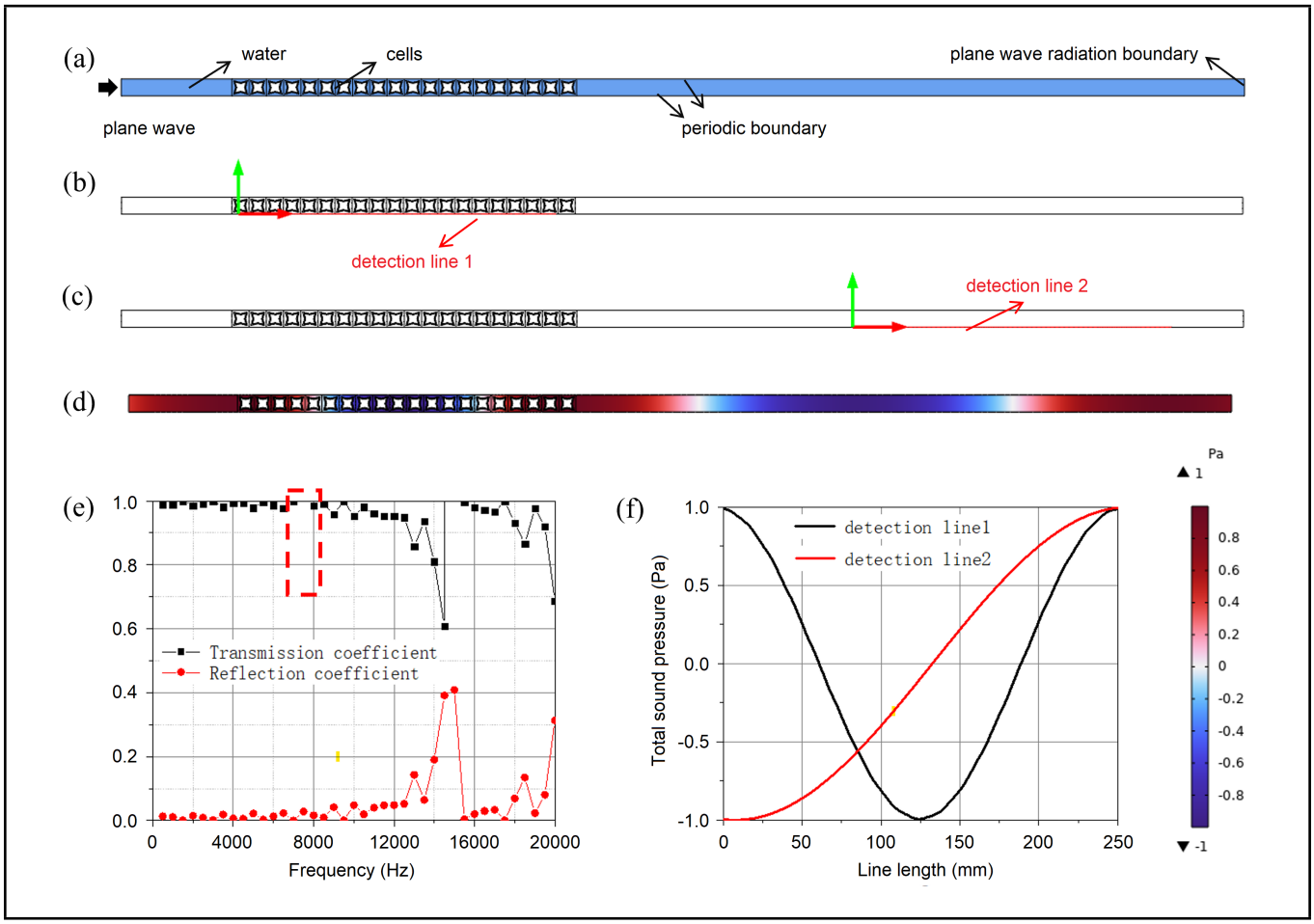

Figure 5. The acoustic waveguide and sound pressure. (a) Sound waves are generated from the left side of the waveguide, traverse through an array consisting of 20 cells, and emerge from the right side. (b) The location and magnification of the observed line within the cell array. (c) The specific position and magnification of the observation line in the water region. (d) The total sound pressure distribution in the acoustic waveguide at 3 kHz. (e) The sound intensity transmission coefficient and reflection coefficient of the cell array. (f) Sound pressure distribution on two observation lines.

cells (depicted as black and red dots in Fig. 5(e)). It illustrates that within the frequency range of $500-7500$ Hz, the array demonstrates minimal sound wave reflection, indicating impedance matching with water. However, transmission gradually decreases in the range of $7500-15000$ Hz, suggesting a gradual mismatch between the array's impedance and water. This observation aligns with the local resonance location on the cell's band curve (Fig. 4(c)). Moreover, it corresponds to the progressive deviation of the band curve slope as frequency increases. Additionally, to validate the slow speed effect, an analysis of sound pressure distribution inside and outside the array in the waveguide using a 3 kHz sound wave as an example was conducted. The wavelength of a 3 kHz sound wave in the water is 0.5 m, while the wavelength of the same frequency in the cell may be 0.25 m. Consequently, an observation line labeled as Line 1 is selected 0.25 mm above the lower boundary of the cell array with a length of 0.25 m, as depicted by the red line in Fig. 5(b). Similarly, an observation line named Line 2 with an equal length is chosen within the water area, illustrated by the red line shown in Fig. 5(c). The overall sound pressure distribution throughout the entire waveguide at 3 kHz can be observed in Fig. 5(d), indicating distinct variations between sound pressure distributions within the array and those within the water area. The sound pressure distributions along both observation lines are displayed in Fig. 5(f). It can be observed that Line 2 corresponds to half a wavelength within the water area, whereas Line 1 corresponds to one full wavelength of a sound wave within the array. Therefore, it can be concluded that the speed of sound within a single cell is half that of the speed of sound within water. By combining this transmission curve with observations made along these two lines regarding sound pressure distribution, it can be proven that the aforementioned unit cell design exhibits impedance matching effect and half the speed of sound in water.

3. CONCLUSIONS

The present study introduces four types of square lattice underwater acoustic metafluid cells, namely AMF1-AMF4, which share the same geometrical parameters but differ in frame thickness and shrinkage factors. Analyzing the band curves, the resonance mode in the low-energy region was defined, and the compression wave mode of the lowest order was examined. The slope of the compression wave mode curve provided an equivalent compression wave velocity for a unit cell, revealing that cells with shrinkage factors generally exhibit lower sound velocities. Considering the obtained equivalent mass density, we also calculated the equivalent volume modulus for the AMF cells. Therefore, it can be seen that the cells containing shrinkage factor generally have lower equivalent volume modulus and sound velocity. Surprisingly, despite having a thicker framework due to its shrinkage factor compared to AMF1 without such a factor, AMF4 still exhibited

a lower volume module. Therefore, the frame shrinkage of an AMF cell made it more prone to shrinkage-expansion deformation, resulting in a decrease in both equivalent volume modulus and equivalent sound velocity and an increase in the equivalent density. Then, we investigated how shrinkage factors affected equivalent parameters through parametric scanning analysis. It was observed that as the shrinkage factor increased, there was a gradual increase in the equivalent density of the cell while the equivalent sound velocity and bulk modulus progressively decreased. Finally, an impedance-matched element was designed, and the sound velocity was 0.5 times that of water by using the low bulk modulus effect caused by the frame shrinkage. By analyzing the transmission and reflection coefficients of the acoustic waveguide containing 20 cells, we have successfully verified the impedance-matching effect of the cell. Additionally, through an analysis of the sound pressure distribution within and outside the cells in the waveguide, it has been confirmed that the cell exhibits a sound velocity equivalent to 0.5 times that of water.

The introduction of the proposed shrinkage frame architecture, which engenders the slow sound phenomenon, augments the structural diversity of acoustic metafluid cells. As a result of this study, there are anticipated reductions in the frame thickness of these cells, enhancements in the fabricability of slow sound entities, and advancements towards the broader application of acoustic metafluid in practice.

REFERENCES

[1] Hoag, D. F., Ingle, V. K., and Gaudette, R. J. Low-bit-rate coding of underwater video using wavelet-based compression algorithms, *IEEE Journal of Oceanic Engineering*, **22** (2), 393–400, (1997). https://doi.org/10.1109/48.585958

[2] Ding, Y., Liu, Z., Qiu, C., and Shi, J. Metamaterial with simultaneously negative bulk modulus and mass density, *Physical Review Letters*, **99** (9), 093904, (2007). https://doi.org/10.1103/PhysRevLett.99.093904

[3] Kildishev, A. V., Boltasseva, A., and Shalaev, V. M. Planar photonics with metasurfaces, *Science*, **339** (6125), (2013). https://doi.org/10.1126/science.1232009

[4] Wu, X., Xia, X., Jingxuan, T., Liu, Z., and Wen, W. Broadband reflective metasurface for focusing underwater ultrasonic waves with linearly tunable focal length, *Applied Physics Letters*, **108**, 163502, (2016). https://doi.org/10.1063/1.4947437

[5] Yang, Y., Wang, H., Yu, F., Xu, Z., and Chen, H. A metasurface carpet cloak for electromagnetic, acoustic and water waves, *Scientific Reports*, **6**, 20219, (2016). https://doi.org/10.1038/srep20219

[6] Zhu, Y., Hu, J., Fan, X., Yang, J., Liang, B., Zhu, X., and Cheng, J. Fine manipulation of sound via lossy metamaterials with independent and arbitrary reflection amplitude and phase, *Nature Communications*, **9** (1), 1632, (2018). https://doi.org/10.1038/s41467-018-04103-0

[7] Bi, Y., Jia, H., Sun, Z., Yang, Y., Zhao, H., and Yang, J. Experimental demonstration of three-dimensional broadband underwater acoustic carpet cloak, *Applied Physics Letters*, **112** (22), 223502, (2018). https://doi.org/10.1063/1.5026199

[8] Chen, J., Rao, J., Lisevych, D., and Fan, Z. Broadband ultrasonic focusing in water with an ultra-compact metasurface lens, *Applied Physics Letters*, **114** (10), 104101, (2019). https://doi.org/10.1063/1.5090956

[9] Hu, C., Yin, Y., and Chen, H. Three-dimensional omnidirectional acoustic illusion, *Physical Review Applied*, **18** (2), 024049, (2022). https://doi.org/10.1103/PhysRevApplied.18.024049

[10] Cai, M., Liu, X., Hu, G., and Zhou, P. Customization of two-dimensional extremal materials, *Materials & Design*, **218**, 110657, (2022). https://doi.org/10.1016/j.matdes.2022.110657

[11] Zhou, P., Jia, H., Bi, Y., Yang, Y., Yang, Y., Zhang, P., and Yang, J. Water-air acoustic communication based on broadband impedance matching, *Applied Physics Letters*, **123** (19), (2023). https://doi.org/10.1063/5.0168562

[12] Huang, M., Zheng, B., Li, R., Shen, L., Li, X., Lu, H., Zhu, R., Cai, T., and Chen, H. Evolutionary games-assisted synchronization metasurface for simultaneous multisource invisibility cloaking, *Advanced Functional Materials*, 2401909, (2024). https://doi.org/10.1002/adfm.202401909

[13] Veselago, V. G. The electrodynamics of substance with simultaneously negative values of ε and μ, *Soviet Physics Uspekhi*, **10** (4), 509, (1968). https://doi.org/10.1070/PU1968v010n04ABEH003699

[14] Lai, Y., Wu, Y., Sheng, P., and Zhang, Z. Q. Hybrid elastic solids, *Nature Materials*, **10** (8), 620–624, (2011). https://doi.org/10.1038/nmat3043

[15] Restrepo-Florez, J. M. and Maldovan, M. Metamaterial membranes, *Journal of Physics D: Applied Physics*, **50** (2), 025104, (2017). https://doi.org/10.1088/1361-6463/50/2/025104

[16] Chen, M., Xu, W., Liu, Y., Yan, K., Jiang, H., and Wang, Y. Band gap and double-negative properties of a star-structured sonic metamaterial, *Applied Acoustics*, **139**, 235–242, (2018). https://doi.org/10.1016/j.apacoust.2018.04.035

[17] Kumar, N. and Pal, S. Low frequency and wide band gap metamaterial with divergent shaped star units: Numerical and experimental investigations, *Applied Physics Letters*, **115** (25), 254101, (2019). https://doi.org/10.1063/1.5119754

[18] Du, Y., Wu, W., Chen, W., Lin, Y., and Chi, Q. Control the structure to optimize the performance of sound absorption of acoustic metamaterial: A review, *AIP Advances*, **11**, 060701,(2021). https://doi.org/10.1063/5.0042834

[19] Xin, Y., Wang, H., Wang, C., Cheng, S., Zhao, Q., Sun, Y., Gao, H., and Ren, F. Properties and tunability of band gaps in innovative reentrant and star-shaped hybrid honeycomb metamaterials, *Results in Physics*, **24**, 104024, (2021). https://doi.org/10.1016/j.rinp.2021.104024

[20] Wen, J., Zhao, H., Lv, L., Yuan, B., and Wen, X. Effects of locally resonant modes on underwater sound absorption in viscoelastic materials, *Journal of the Acoustical Society of America*, **130** (3), 1201–1208, (2011). https://doi.org/10.1121/1.3621074

[21] Meng, H., Wen, J., Zhao, H., and Wen, X. Optimization of locally resonant acoustic metamaterials on underwater sound absorption characteristics, *Journal of Sound and Vibration*, **331** (20), 4406–4416, (2012). https://doi.org/10.1016/j.jsv.2012.05.027

[22] Chen, M., Meng, D., Zhang, H., Jiang, H., and Wang, Y. Resonance-coupling effect on broad band gap formation in locally resonant sonic metamaterials, *Wave Motion*, **63**, 111–119, (2016). https://doi.org/10.1016/j.wavemoti.2016.02.003

[23] Cai, X., Wang, L., Zhao, Z., Zhao, A., Zhang, X., Wu, T., and Chen, H. The mechanical and acoustic properties of two-dimensional pentamode metamaterials with different structural parameters, *Applied Physics Letters*, **109** (13), 131904, (2016). https://doi.org/10.1063/1.4963818

[24] Amendola, A., Smith, C. J., Goodall, R., Auricchio, F., Feo, L., Benzoni, G., and Fraternali, F. Experimental response of additively manufactured metallic pentamode materials confined between stiffening plates, *Composite Structures*, **142**, 254-262, (2016). https://doi.org/10.1016/j.compstruct.2016.01.091

[25] Fabbrocino, F., Amendola, A., Benzoni, G., and Fraternali, F. Seismic application of pentamode lattices, *Ingegneria Sismica*, **1**, 62–71, (2016).

[26] Zhao, A., Zhao, Z., Zhang, X., Cai, X., Wang, L., Wu, T., and Chen, H. Design and experimental verification of a water-like pentamode material, *Applied Physics Letters*, **110** (1), 011907, (2017). https://doi.org/10.1063/1.4973924

[27] Mohammadi, K., Movahhedy, M. R., Shishkovsky, I., and Hedayati, R. Hybrid anisotropic pentamode mechanical metamaterial produced by additive manufacturing technique, *Applied Physics Letters*, **117** (6), 061901, (2020). https://doi.org/10.1063/5.0014167

[28] Chu, Y., Wang, Z., and Xu, Z. Broadband high-efficiency controllable asymmetric propagation by pentamode acoustic metasurface, *Physics Letters A*, **384** (11), 126230, (2020). https://doi.org/10.1016/j.physleta.2019.126230

[29] Cushing, C. W., Kelsten, M. J., Su, X., Wilson, P. S., Haberman, M. R., and Norris, A. N. Design and characterization of a three-dimensional anisotropic additively manufactured pentamode material, *The Journal of the Acoustical Society of America*, **151** (1), 168–179, (2022). https://doi.org/10.1121/10.0009161

[30] Layman, C. N., Naify, C. J., Martin, T. P., Calvo, D. C., and Orris, G. J. Highly-anisotropic elements for acoustic pentamode applications, *Physical Review Letters*, **111** (2), 024302, (2013). https://doi.org/10.1103/PhysRevLett.111.024302

[31] Schittny, R., Bückmann, T., Kadic, M., and Wegener, M. Elastic measurements on macroscopic three-dimensional pentamode metamaterials, *Applied Physics Letters*, **103** (23), 231905, (2013). https://doi.org/10.1063/1.4838663

[32] Zhang, L., Song, B., Zhao, A., Liu, R., and Shi, Y. Study on mechanical properties of honeycomb pentamode structures fabricated by laser additive manufacturing: Numerical simulation and experimental verification, *Composite Structures*, **226**, 111199, (2019). https://doi.org/10.1016/j.compstruct.2019.111199

[33] Norris, A. N. Acoustic cloaking in 2D and 3D using finite mass, *Physics*, (2008). https://doi.org/10.48550/arXiv.0802.0701

[34] Tian, Y., Wei, Q., Cheng, Y., Xu, Z., and Liu, X. Broadband manipulation of acoustic wavefronts by pentamode metasurface, *Applied Physics Letters*, **107** (22), 221906, (2015). https://doi.org/10.1063/1.4936762

[35] Chen, Y., and Hu, G. Broadband and high-transmission metasurface for converting underwater cylindrical waves to plane waves, *Physical Review Applied*, **12** (4), 044046, (2019). https://doi.org/10.1103/PhysRevApplied.12.044046

[36] Cushing, C. W., Haberman, M. R., Wilson, P. S., Su, X., and Norris, A. N. Experimental validation of the underwater sound focusing properties of a pentamode gradient index metamaterial lens, *The Journal of the Acoustical Society of America*, **140** (4), 3048, (2016). https://doi.org/10.1121/1.4969471

[37] Zhang, X., Chen, H., Zhao, Z., Zhao, A., and Wang, L. Experimental demonstration of a broadband waterborne acoustic metasurface for shifting reflected waves, *Journal of Applied Physics*, **127** (17), 174902, (2020). https://doi.org/10.1063/1.5139008

[38] Zhao, A., Jia, H., Zhang, M., Wang, Z., Zhou, P., Liu, C., Zhao, Z., Zhang, X., Wu, T., Chen, H., Liu, B., and Song, B. Design and experimental verification of a broadband multiphase pentamode material, *Physical Review Applied*, **18** (3), 034001, (2022). https://doi.org/10.1103/PhysRevApplied.18.034001

[39] Zhou, P., Jia, H., Bi, Y., Liao, B., Yang, Y., Yan, K., Zhang, J., and Yang, J. Underwater carpet cloak for broadband and wide-angle acoustic camouflage based on three-component metafluid, *Physical Review Applied*, **18** (1), 014050, (2022). https://doi.org/10.1103/PhysRevApplied.18.014050

[40] Bi, Y., Zhou, P., Jia, H., Lu, F., Yang, Y., Zhang, Y., Zhang, P., and Yang, J. Acoustic metafluid for independent manipulation of the mass density and bulk modulus. *Materials & Design*, **233**, 112248, (2023). https://doi.org/10.1016/j.matdes.2023.112248